Supporting Information

for

Phase-pure $MAPbBr_3$ Thin Films Prepared by Room-Temperature Powder Aerosol Deposition (PAD) and Their Optical and Electrical Properties

Tianshan Xu[1], Markus Griesbach[2], Till Scholz[1], Daniel Paulus[1], Martin Hämmerle[1], Anna Köhler[2], Ralf Moos[1,] *

[1]Department of Functional Materials, University of Bayreuth, 95440, Bayreuth, Germany

[2]Soft Matter Optoelectronics, Department of Physics, and Bayreuth Institute of Macromolecular Research (BIMF), and Bavarian Polymer Institute (BPS), University of Bayreuth, 95440 Bayreuth, Germany

*Corresponding author

Correspondence to: functional.materials@uni-bayreuth.de; Tel.:+49 (0)921 55 7401

Table of content

S1. Powder Aerosol Deposition

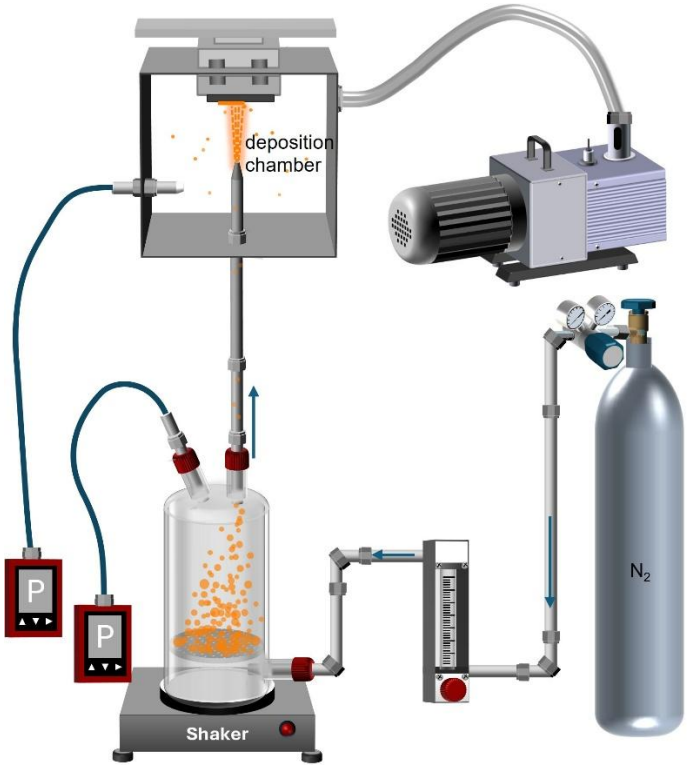

Fig. S1: Schematic illustration of the powder aerosol deposition (PAD) setup without the use of an ejector–separator unit and without an inertial separator having a collecting tube

Film Thickness and Morphology of $MAPbBr_3$ Films

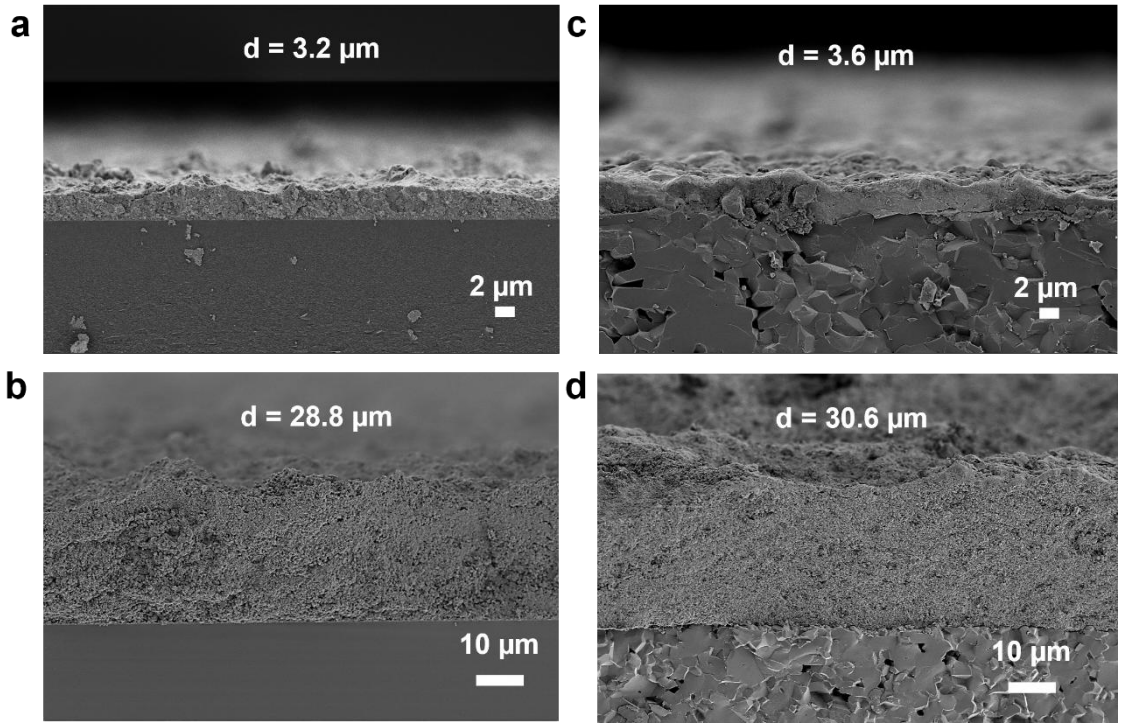

Fig. S2: Cross-sectional SEM images of aerosol-deposited $MAPbBr_3$ films on different substrates. Films deposited on SnO_2-coated ITO glass substrates with **a** 2 scans and **b** 20 scans, and on C-IDEs patterned Al_2O_3 substrates with **c** 2 scans and **d** 20 scans. The film thickness is indicated in each image.

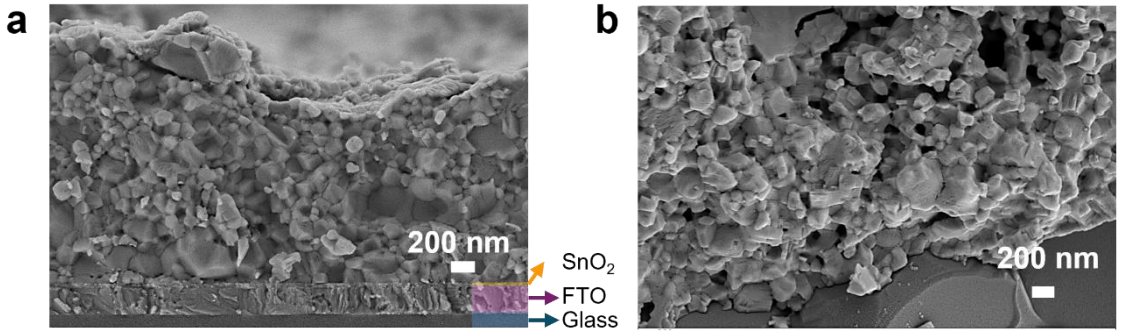

Fig. S3: Cross-sectional SEM images of the film-substrate interface for aerosol-deposited $MAPbBr_3$ films on different substrates: **a** on a SnO_2-coated ITO glass substrate and **b** on an Al_2O_3 substrate. Colored arrows in **a** indicate the SnO_2 layer (orange), the ITO layer (purple), and the glass substrate (blue).

S2. Optical Measurements

Reproducibility

The optical properties in perovskites are highly sensitive to local inhomogeneities. To assess the uniformity of our samples, we recorded photoluminescence (PL) spectra at several spots of the film, exemplary shown in **Fig. S4a**. We found the spectral shape is independent of the excitation spot, indicating a high degree of homogeneity. The intensity across the different spots varies by approximately 10%, which may be attributed to geometric factors such as the rough, inhomogeneous surface texture of the films.

To evaluate the reproducibility of the PAD process, we fabricated three films from the same powder batch under identical conditions. The resulting samples exhibit comparable thicknesses of approximately 4.5-5.5 µm, and their emission spectra, shown in **Fig. S4b**, are nearly identical, confirming good reproducibility.

It should be noted that the excitation spot size used in the quasi-steady-state PL measurements in this work is relatively large (0.0255 cm^2). As a result, inhomogeneities occurring on small length scales are spatially averaged and do not significantly influence the measured emission spectra.

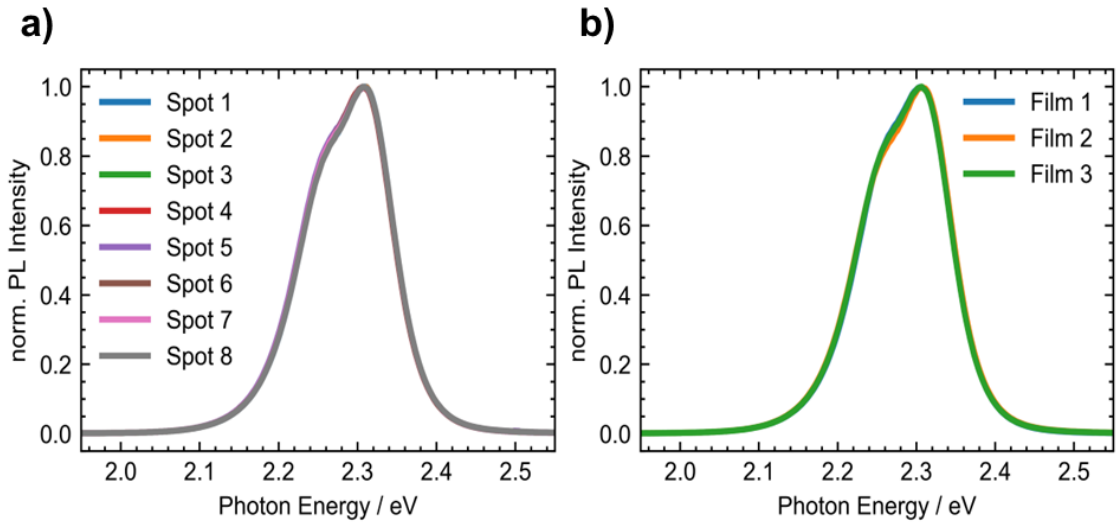

Fig. S4: Reproducibility of quasi-steady-state PL measurements: **a** Spectra recorded at different illumination spots of a PAD film. **b** Spectra of different PAD films with similar thickness synthesized under identical conditions from the same batch of $MAPbBr_3$ powder. All spectra were recorded using a fluence of 11 µJ/cm^2.

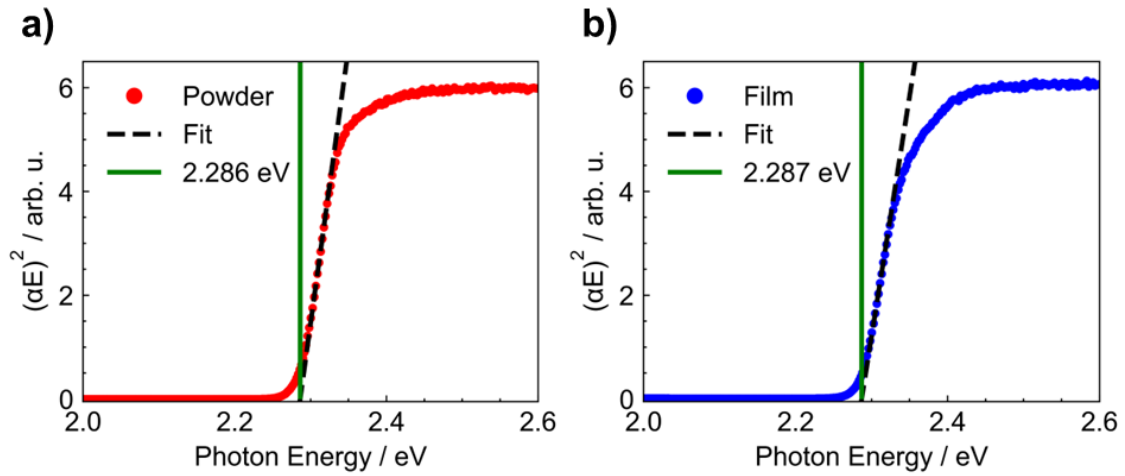

Fig. S5: Tauc-plots of a representative **a** powder sample and **b** thin film. Fits to the linear region are indicated by black dashed lines. The intersects of these lines with the abscissa mark the Tauc-bandgaps, highlighted by green lines.

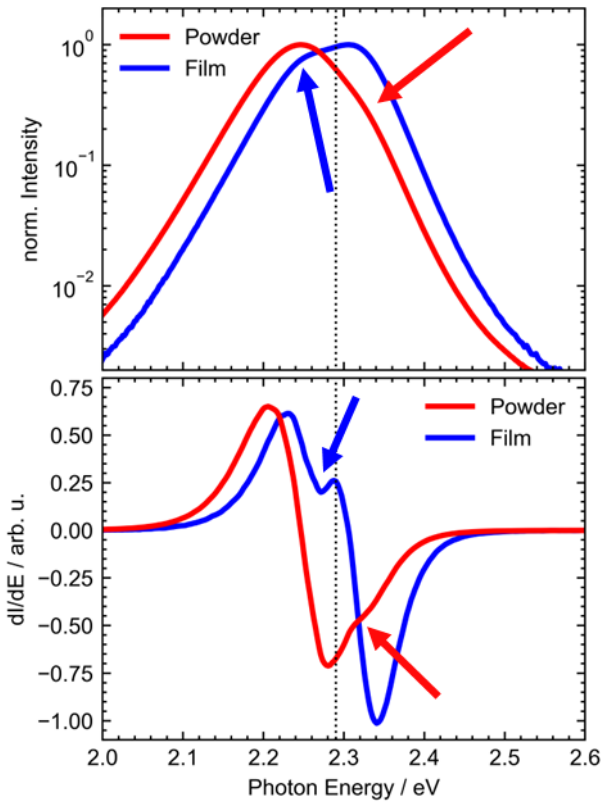

Fig. S6: PL spectra from **Fig. 6b** of film and powder in semilogarithmic depiction (top) and their derivate with respect to energy (bottom). The coloured arrows indicate the positions of the respective shoulders at higher (powder) and lower energy (film) compared to the main peaks. The dotted line marks the Tauc-derived absorption onset. The spectra were recorded under a fluence of 11 µJ/cm².

Deconvolution of PL Spectra

To deconvolute the structured emission spectra, we found that a simple sum of two Gaussian functions is inadequate to model the observed spectral shape, especially the low energy flank. Instead, we used the Lasher-Stern-Würfel equation (**Eq. S1**) [1] to describe the shape of the PL emission peaks, $I_{PL}(E)$, approximating the absorption with an Urbach tail and constant absorption above the bandgap:

$$I_{PL}(E) = \mathrm{A} \cdot E^2 \exp\left(-\frac{E}{k_B T}\right)\left[\exp\left(-\frac{E - E_0}{E_U}\right) + 1\right]^{-1} \qquad \text{(Eq. S1)}$$

Here, E_U is the Urbach energy, E_0 a characteristic energy value close to the bandgap, $k_B T$ the thermal energy and A is a scale factor. The total PL emission in our model is then simply given by **Eq. S2** as a sum of two peaks described by **Eq. S1**. To reduce the number of free parameters, we kept E_U and T identical for the two peaks, allowing only variation of the amplitudes A_i and positions $E_{0,\mathrm{i}}$ (with i = 1, 2). We note that $E_{0,\mathrm{i}}$ is not equivalent to energy where the function reaches its maximum value. This additionally depends on T and E_U, but since these two parameters only vary slightly in our measurements, changes in the position of the maximum are dominated by $E_{0,\mathrm{i}}$. Therefore, we will simply referred to $E_{0,\mathrm{i}}$ as the respective peak position in the following.

$$I_{ges}(E) = E^2 \exp\left(-\frac{E}{k_B T}\right)\left\{\mathrm{A}_1\left[\exp\left(-\frac{E - E_{0,1}}{E_U}\right) + 1\right]^{-1} + \mathrm{A}_2\left[\exp\left(-\frac{E - E_{0,2}}{E_U}\right) + 1\right]^{-1}\right\} \qquad \textbf{(Eq. S2)}$$

Fig. S7 shows the PL spectra of a thin film sample deconvoluted in the manner described at different excitation fluences. The complete list of the fitting parameters at all fluences can be found in **Table ST1**. Interestingly, we find that the position of the higher energy peak, characterized by $E_{0,2}$, decreases with increasing fluence. Fitting the spectra with one $E_{0,2}$ optimized globally across the measurements at all fluences (while letting the other parameters vary freely) was insufficient to describe the experimental observations, as can be seen in **Fig. S8**.

The deconvolution of the powder spectra at different fluences was performed in the same matter. The spectra and fits are shown in **Fig. S9**, and the full list of fitting parameters is provided in **Table ST2**.

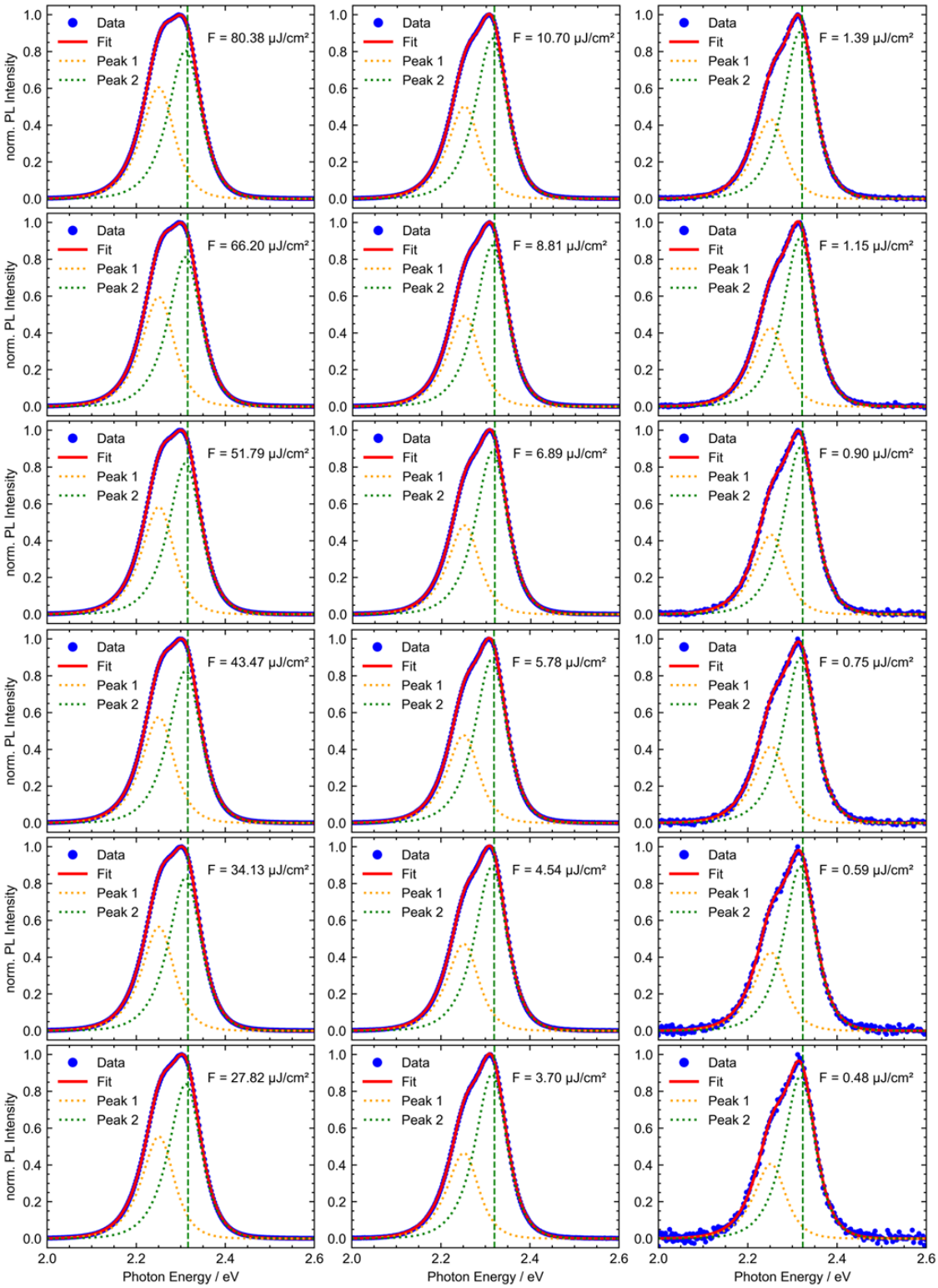

Fig. S7: PL spectra of an aerosol-deposited thin film sample at different excitation fluences, alongside deconvolution into two peaks by fitting the spectra according to **Eq. S2**. The position of the higher energy peak is marked by vertical green dashed lines. The spectra at fluences of 80.38 µJ/cm², 10.70 µJ/cm² and 1.39 µJ/cm² correspond to the measurements shown in **Fig. 6** of the main manuscript, where the fluence was rounded considering experimental uncertainty.

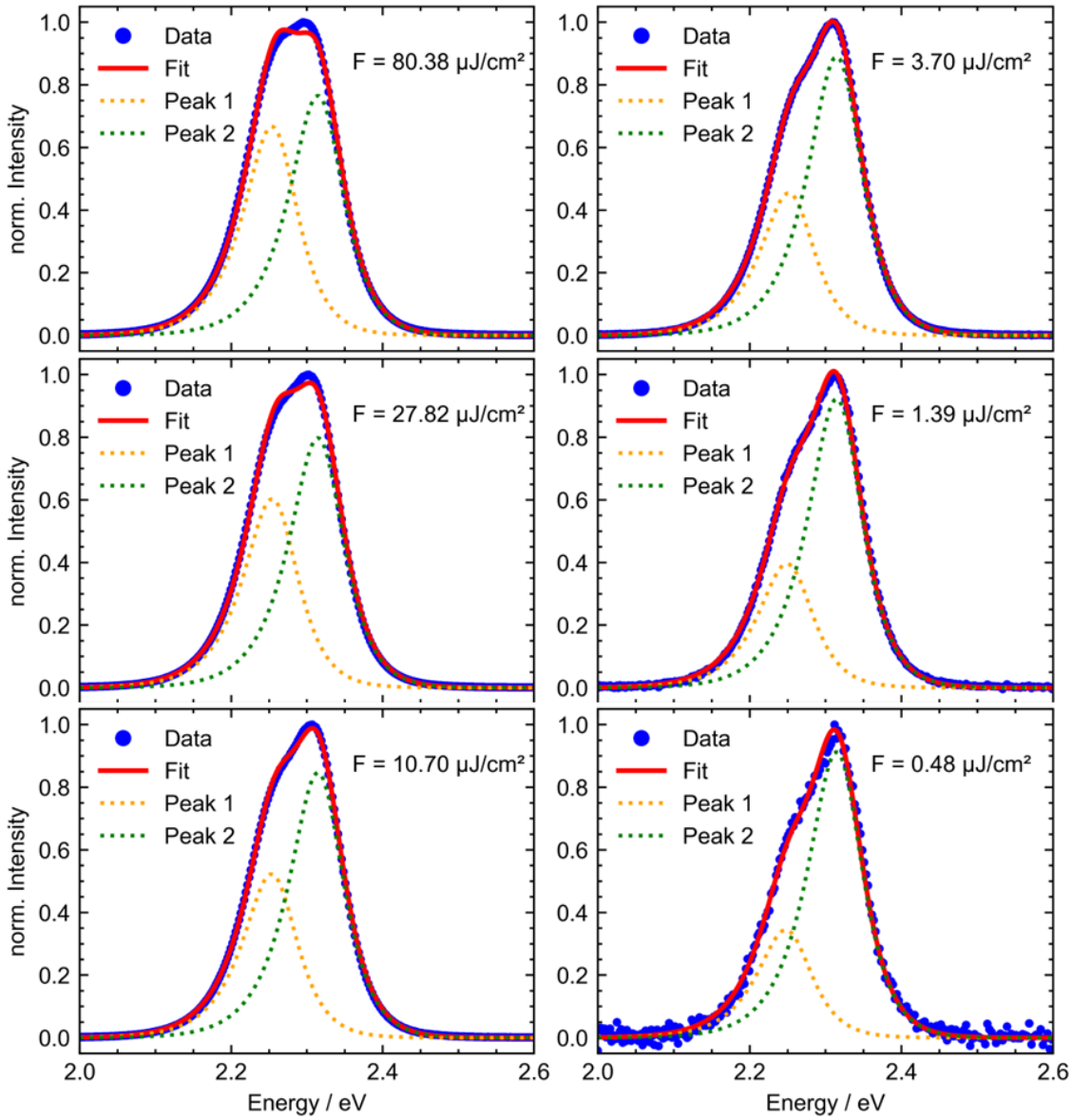

Fig. S8: Deconvolution of the PL spectra of a thin film using a fixed position for the higher energy peak, shown exemplary at selected excitation fluences. The used value of $E_{0,2} = 2.320$ eV was determined from global optimization across measurements at all fluences. As can be seen, this model reproduces the spectra well at intermediate fluences of ~1-11 µJ/cm² but deviates at the extremes: at very low (very high) fluences the position of the high energy peak is too low (too high) to accurately capture the experimental data. Because of this systematic mismatch, we decided to let $E_{0,2}$ vary freely across fluences.

Table ST1: Fitted parameters according to **Eq. S2** for the PL spectra of a thin film at different fluences.

Fluence / µJ/cm²	$A_1/(A_1+A_2)$	$A_2/(A_1+A_2)$	$E_{0,1}$ / eV	$E_{0,2}$ / eV	E_U / meV	T / K
80.38	0.43	0.57	2.255	2.315	16.2	320
66.20	0.42	0.58	2.255	2.315	16.1	319
51.79	0.42	0.58	2.255	2.315	16.1	317
43.47	0.41	0.59	2.255	2.316	16.0	316
34.13	0.40	0.60	2.255	2.316	16.0	315
27.82	0.40	0.60	2.256	2.316	15.9	313
10.70	0.37	0.63	2.256	2.318	15.8	308
8.81	0.36	0.64	2.256	2.318	15.7	307
6.89	0.35	0.65	2.256	2.319	15.7	307
5.78	0.35	0.65	2.256	2.319	15.7	306
4.54	0.35	0.65	2.256	2.319	15.7	306
3.70	0.34	0.66	2.257	2.320	15.7	304
1.39	0.32	0.68	2.256	2.322	15.6	304
1.15	0.32	0.68	2.256	2.322	15.6	304
0.90	0.32	0.68	2.257	2.323	15.5	300
0.75	0.32	0.68	2.258	2.323	15.5	299
0.59	0.32	0.68	2.256	2.323	15.6	304
0.48	0.32	0.68	2.257	2.323	15.5	302

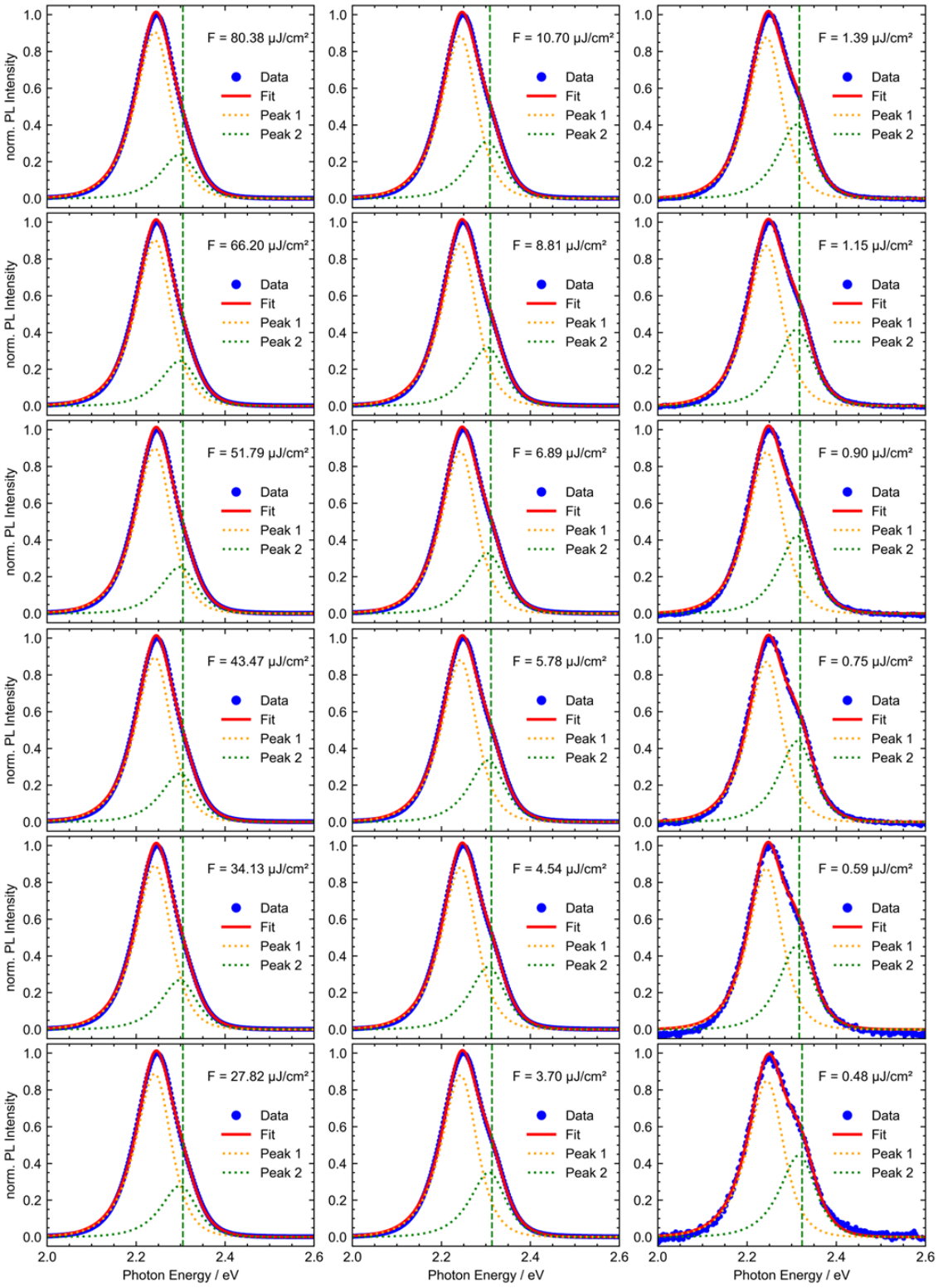

Fig. S9: PL spectra of a powder at different excitation fluences, alongside deconvolution into two peaks by fitting the spectra according to **Eq. S2**. The position of the higher energy peak is marked by vertical green dashed lines. The spectrum at a fluence of 10.70 µJ/cm² corresponds to the measurement shown in **Fig. 6** of the main manuscript, where the fluence was rounded considering experimental uncertainty.

Table ST2: Fitted parameters according to **Eq. S2** for the PL spectra of a powder sample at different fluences. For the powder, the parameter T exhibited a large error but little impact on the fit. To allow for a more meaningful comparison, we fixed it to 330 K, near the global optimum across all fluences.

Fluence / μJ/cm²	$A_1/(A_1+A_2)$	$A_2/(A_1+A_2)$	$E_{0,1}$ / eV	$E_{0,2}$ / eV	E_U / meV	T / K
80.38	0.79	0.21	2.248	2.305	17.4	330
66.20	0.79	0.21	2.248	2.305	17.4	330
51.79	0.78	0.22	2.248	2.305	17.4	330
43.47	0.77	0.23	2.248	2.305	17.4	330
34.13	0.77	0.23	2.248	2.305	17.4	330
27.82	0.76	0.24	2.248	2.305	17.3	330
10.70	0.74	0.26	2.249	2.309	17.3	330
8.81	0.73	0.27	2.249	2.310	17.3	330
6.89	0.73	0.27	2.249	2.311	17.3	330
5.78	0.72	0.28	2.249	2.311	17.3	330
4.54	0.72	0.28	2.249	2.312	17.3	330
3.70	0.71	0.29	2.249	2.313	17.3	330
1.39	0.69	0.31	2.250	2.317	17.3	330
1.15	0.68	0.32	2.249	2.317	17.2	330
0.90	0.68	0.32	2.250	2.318	17.1	330
0.75	0.66	0.34	2.249	2.319	17.1	330
0.59	0.66	0.34	2.248	2.317	16.7	330
0.48	0.66	0.34	2.251	2.323	17.4	330

The extracted fit parameters for powder and thin film in dependence on excitation fluence show several notable trends, depicted in **Fig. S10**. Firstly, the position of the lower energy peak, given by $E_{0,1}$, does not change significantly with excitation fluence for both sample types (**Fig. S10a**), but its absolute value is about 10 meV higher in the thin film. Meanwhile, the position of the higher energy peak ($E_{0,2}$), decreases with increasing fluence for both samples (**Fig. S10b**). Once again, we observe an offset of about 10 meV between powder and film, which decreases at lower fluences. At high fluences (>20 µJ/cm²), $E_{0,2}$ for the powder appears to plateau, however, this may also be a result of the reduced distinguishability of the higher energy peak under these excitation conditions.

A second observation concerns the Urbach energy. For the powder, it remains approximately constant, whereas for the thin film it shows a slight decrease with decreasing fluence (**Fig. S10c**). We attribute this to a fluence-dependent flattening of the high energy flank in the thin film sample, which leads to an apparent increase the fitted temperature [2]. Correcting the Urbach energy for this effect using **Eq. S3** with the actual temperature (T_{actual} = 300 K) at which the measurements were performed, largely removes the apparent fluence dependence as can be seen in **Fig. S10d**. The physical origin of this high energy flank flattening at higher fluences is not entirely clear as of now.

$$E_{U,corr} = \left[\frac{1}{E_U} + \frac{1}{k_B}\left(\frac{1}{T_{actual}} - \frac{1}{T}\right)\right]^{-1} \qquad \textbf{(Eq. S3)}$$

A third observation is related to the relative contribution of the two peaks, given by the ratio of the amplitude parameters A_1 and A_2. In the powder sample, the contribution of the lower energy peak (A_1) is significantly higher than in the film. For both samples, the relative contribution of the higher energy peak increases at decreasing fluences, in a similar fashion (**Fig. S10e**). This becomes clearer when considering the relative change in the ratio A_1/A_2 compared to its value at the highest fluence (**Fig. S10f**).

As mentioned in the main manuscript, the two most common explanations for structured PL emission in $MAPbBr_3$ invoke either simultaneous radiative recombination from excitons and free carriers or self-absorption effects. In both cases, the higher energy peak would originate from direct recombination of free electrons and holes. We find that for both film and powder, the relative contribution of the higher energy peak increases at lower fluences. In the exciton picture, this would be rationalized by the increasing population of excitons compared to free carriers at high charge carrier densities in accordance with the trend expected from Saha's equation. The absolute values are dependent on the radiative recombination rates of excitons and free carriers and the formalism is only valid at thermal equilibrium, which is not the case in the quasi-steady-state PL measurements employed in this work. Therefore, it is not easily possible to calculate these values without further far-reaching assumptions, but the general trend of increased low-energy contribution at high fluences matches with what would be expected in the exciton and free carrier picture. In contrast, if the structured PL is the result of self-absorption effects

only, the increased prominence of the higher energy “direct” emission peak in relation to the “filtered” peak at low fluences is harder to explain.

However, the opposite is true regarding the large discrepancy in the ratio of the two peaks between the film and the powder. In the powder, the lower energy peak dominates the spectrum, and the higher energy peak appears only as a slight shoulder, while in the film the higher energy peak has a higher intensity than the lower energy peak. If the two peaks were solely the result of distinct excitonic and free carrier recombination, we would not expect such a strong dependence on the sample type. Meanwhile, self-absorption effects are expected to be quite distinct depending on sample geometry. Such considerations would also explain the apparent energetic offset of ~10 meV of the lower energy peak between powder and film.

The apparent redshift of the higher energy peak in both sample types with increasing fluence is highly unusual. If anything, the optical transition is expected to occur at higher energies at higher charge carrier concentration due to Burnstein-Moss band filling effects [3–5]. Yet, as can be seen in **Fig. S8**, a shift towards lower energies with increasing fluence is necessary to capture the experimental observations with the simple two peak model (**Eq. S2**). To fully explain this feature, it might be necessary to further expand this model e.g. by modelling the charge carrier distribution within the sample, which is beyond the scope of this work.

In addition, the notable offset of the energetic position of the higher energy peak ($E_{0,2}$) assumed to correspond to band-to-band emission between thin film and powder is initially surprising. One possible explanation may be the generally smaller crystallite size in the film (see next section).

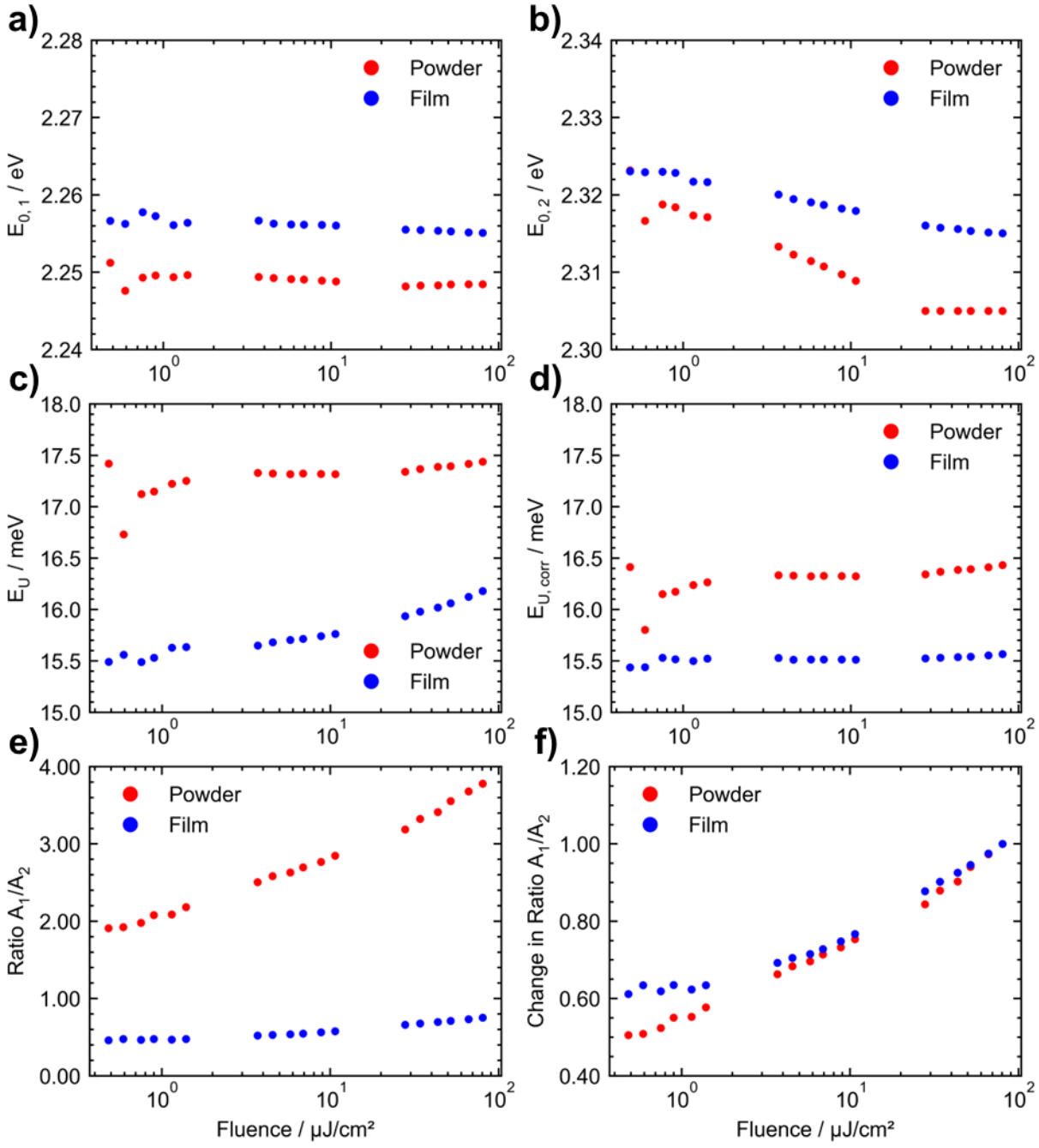

Fig. S10: Fitted parameters according to **Eq. S2** for the PL spectra of a thin film and powder sample as a function of excitation fluence. **a** Position of the lower energy peak, **b** position of the higher energy peak, **c** Urbach energy, **d** temperature-corrected Urbach energy following **Eq. S3**, **e** amplitude ratio of lower and higher energy peaks and **f** change in amplitude ratio normalized to the value at the highest measured fluence.

Backside Illumination

To further characterize our samples, we also measured the PL emission spectrum when illuminating the backside of the thin films, i.e. through the ITO-substrate. The resulting spectrum alongside its deconvolution is shown in **Fig. S10**. While the resulting fit parameters of Urbach energy (15.7 meV), Temperature (309 K) and position of the low energy peak (2.253 eV) are almost identical to the results from frontside illumination under the same excitation conditions (see **Table ST1**), the position of the second peak (2.329 eV) is shifted by about 10 meV. One possible explanation for this observation could be a difference in crystallite size. It has been reported that smaller crystallites exhibit a bandgap increase, which has been attributed to a distortion of the Pb-Halide bond [6,7]. In general, the film exhibits a smaller crystallite size than the powder (see e.g. **Fig. 7**), which may account for the blueshifted higher energy peak. Following this line of thought, it is plausible that the perovskite layer at the very bottom of the film, compressed by aerosol deposition of subsequent layers, consists of smaller crystallites than the layer on top, which is probed by frontside illumination. However, for now this interpretation remains tentative, as other effects such as the exposure of the frontside to atmosphere and the ITO-perovskite interface may also play a role. Further investigation is required to determine the origin of this effect with certainty.

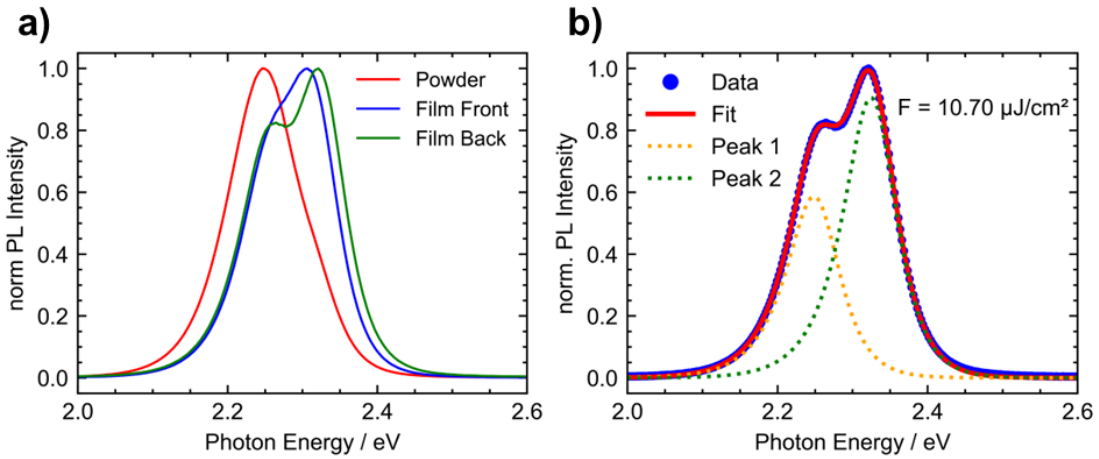

Fig. S11: a Comparison of the emission spectrum of a powder, a film from the frontside and the same film from the backside. **b** Deconvolution of a thin film spectrum under backside illumination according to **Eq. S2**.

Dependence on Film Thickness

The thin film samples used for the optical characterization in the main manuscript and until now in the SI have comparable thicknesses of approximately 5 µm. To investigate any possible influence of the film thickness on the structured emission, we fabricated aerosol-deposited films with thicknesses of 2 µm and 7 µm. The emission spectra of these samples are shown in **Fig. S12a**. The spectrum of the thicker 7 µm film is very similar to that of the 5 µm film, but the lower energy shoulder occurs at slightly lower energies. On the first glance, the emission spectrum of the thinner 2 µm film looks quite different, with only one clear emission peak. Closer examination reveals that the emission spectrum cannot be described well when using only one peak according to **Eq. S1**. A satisfactory fit of the spectrum, shown in **Fig. S12b**, once again requires the use of two peaks using **Eq. S2**. Notably, the position of the higher energy peak at approximately 2.32 eV is consistent across all three samples, while the position of the lower energy peak decreases with increasing film thickness (2 µm: 2.28 eV, 5 µm: 2.26 eV, 7 µm: 2.25 eV).This observations is difficult to rationalize if excitonic recombination is the origin of the lower energy peak and band-to-band recombination the origin of the higher energy peak. Meanwhile, self-absorption effects, which are naturally dependent on the sample thickness, would be expected to lead to such behaviour. Therefore, we conclude that the structured emission observed in our samples is most likely the result of prominent self-absorption effects.

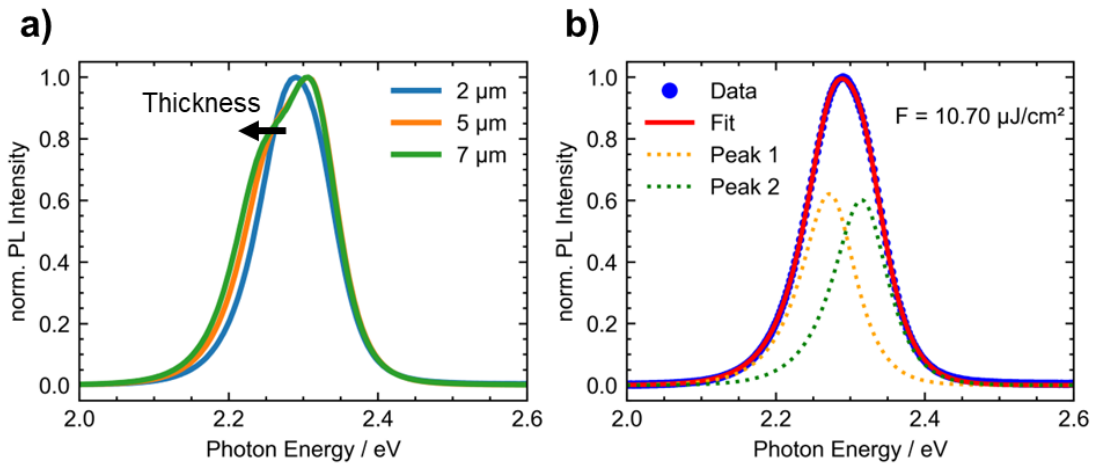

Fig. S12: a Emission spectra for PAD films of differing thickness recorded using a fluence of ~11 µJ/cm². The black arrow indicates the redshift of the lower energy shoulder with increasing thickness. **b** Exemplary deconvolution of spectrum of the 2 µm film according to **Eq. S2**.

S3. Time-resolved Photoluminescence

If radiative recombination of free carriers is the dominant mechanism in a semiconductor, the PL intensity as a function of time is proportional to the product of the concentration of free electrons (n) and holes (p) minus the square of the intrinsic charge carrier concentration n_i:

$$I_{PL}(t) \propto n(t) \cdot p(t) - {n_i}^2 \quad \textbf{(Eq. S4)}$$

Neglecting diffusion (which happens at very fast timescales), Auger recombination (which is only relevant at extremely high charge carrier concentrations) and photon recycling events, the time evolution of the charge carrier concentrations in the presence of one relatively shallow trap (i.e. a trap state where thermal emission back into the band is not completely negligible) for electrons can be written as:

$$\frac{dn}{dt} = -\frac{n}{\tau_{bulk,n}} - k_{rad}(np - {n_i}^2) - \beta_n \cdot n \cdot (N_T - n_T) + e_n \cdot n_T \quad \textbf{(Eq. S5)}$$

$$\frac{dp}{dt} = -\frac{p}{\tau_{bulk,p}} - k_{rad}(np - {n_i}^2) - \beta_p \cdot n \cdot n_T + e_p \cdot (N_T - n_T) \quad \textbf{(Eq. S6)}$$

We note that this description is equally valid for systems dominated by hole traps, when simply switching the roles of n and p. The first term in both equations represents recombination via deep traps in the bulk, which was found to be not relevant in our case, i.e. $\tau_{bulk,p} \sim \tau_{bulk,n} \sim \infty$. The second term describes the radiative recombination of electrons and holes. The radiative recombination rate, k_{rad}, is a material constant and was assumed to be $5 \cdot 10^{-10}$ cm³/s [8]. The third term accounts for the capture of a charge carrier in a trap. $\beta_{n,p}$ are the capture coefficients, N_T is the trap density and n_T the density of occupied traps. The last term reflects the thermal remission of trapped carriers back into the band, described by the thermal emission rates $e_{n,p}$. These are given by:

$$e_n = \beta_n N_C \exp\left(-\frac{E_g - E_T}{k_B T}\right) \quad \textbf{(Eq. S7)}$$

$$e_p = \beta_p N_V \exp\left(\frac{-E_T}{k_B T}\right) \quad \textbf{(Eq. S8)}$$

Here, N_C and N_V are the effective densities of states of the conduction and valence bands, which we both assumed to be $2.8 \cdot 10^{18}$ cm^{-3} [9]. E_g is the band gap energy and E_T the energy of the trap state relative to the valence band. We used a value of 2.315 eV for the band gap in line with the position of the high energy PL peak instead of the Tauc-derived absorption onset, since the latter is not indicative of the intrinsic bandgap due to excitonic absorption contributions. We note that only the relative value of $E_g - E_T$ is relevant, since the thermal emission of holes, (i.e. the thermal capture of a valence band electron by an empty trap) is negligible at room temperature ($e_p \approx 0$).

Following **Eqs. S5** and **S6**, the evolution of the concentration of trapped electrons is given by:

$$\frac{dn_T}{dt} = \beta_n \cdot n \cdot (N_T - n_T) - e_n \cdot n_T - \beta_p \cdot n \cdot n_T + e_p \cdot (N_T - n_T) \qquad \textbf{(Eq. S9)}$$

The first term corresponds to the capture of an electron by an empty trap, the second term describes the thermal emission of a trapped electron into the conduction band, the third term accounts for hole capture by an occupied trap, i.e. trap-assisted recombination, and the last term covers the possibility of a valence band electron being thermally excited into a trap, i.e. the thermal emission of a hole.

We used a custom python script based upon an existing MATLAB script published by Yuan *et al.* [10] to simulate the TRPL decay and optimize the parameters. We estimated the initial charge carrier concentration $n(0) = p(0) = n_0 + n_i$ from the excitation fluence to be $5 \cdot 10^{17}$ cm^{-3}. The equilibrium concentration of trapped carriers $n_T(0)$ was calculated by using an iterative approach. $n_T(0)$ is estimated by the Fermi-Dirac occupation (initial Fermi-energy $E_f \approx E_g/2$), then p is calculated by utilizing the charge neutrality condition ($n + n_T = p$) and mass-action relation ($np = {n_i}^2$). Then the Fermi-energy is recalculated using the canonical formula ($E_f = k_B T \cdot \log(N_V/p)$) and the calculation is repeated until the Fermi-energy converges.

Table ST3 lists all parameters used in the modelling of the TRPL data. The optimized fit is shown as a red line in **Fig. 9**.

Table ST3: Rate equation model parameters used for fitting the data in **Fig. 9**. Only β_n, β_p, N_T and E_T were varied, the remaining parameters were kept constant.

Parameter	Value	Fitted?
Bandgap energy E_g	2.315 eV	No
Density of states $N_C = N_V$	2.8e18 cm^{-3}	No
Intrinsic charge carrier concentration n_i	4.5e10 cm^{-3}	No
Radiative recombination rate k_{rad}	5e-10 cm^3/s	No
Temperature T	300 K	No
Initial charge carrier concentration n_0	5e17 cm^{-3}	No
Capture rate of electrons β_n	1.5e-10 cm^3/s	Yes
Capture rate of holes β_p	8.6e-10 cm^3/s	Yes
Trap density N_T	1.62e18 cm^{-3}	Yes
Trap energy E_T (relative to valence band)	2.198 eV	Yes

S4. Structural and Microstructural Properties After Annealing

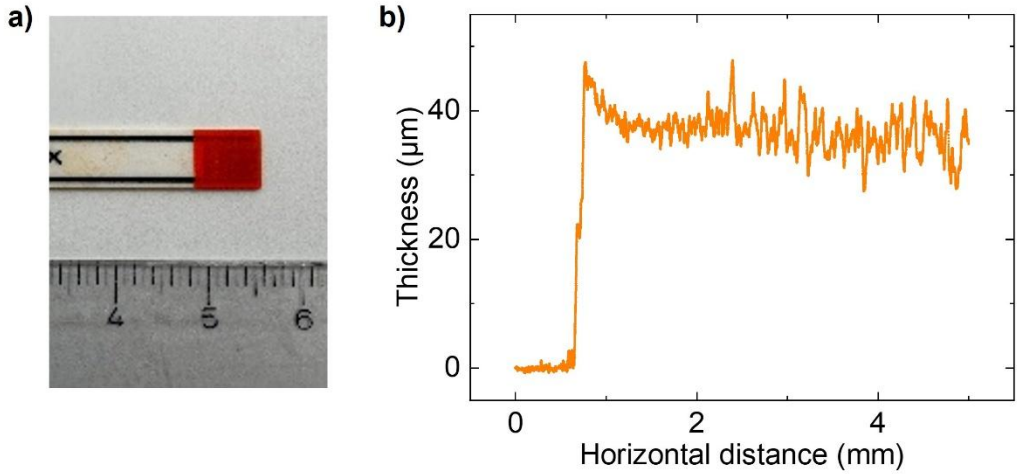

Fig. S13: a Photograph of a PAD-MAPbBr$_3$ film on an Al_2O_3 substrate with carbon interdigital electrodes (IDE). **b** Lateral thickness profile measured across the film

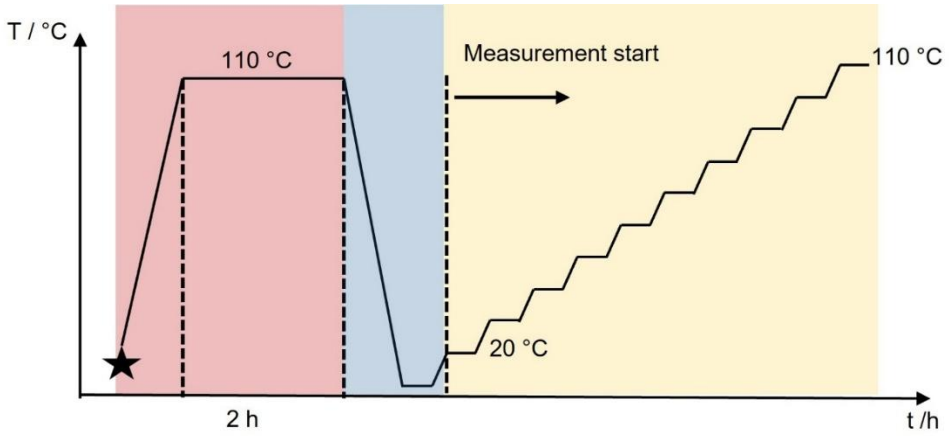

Fig. S14: Temperature profile of the annealing process followed by a measurement series from 20 to 110 °C.

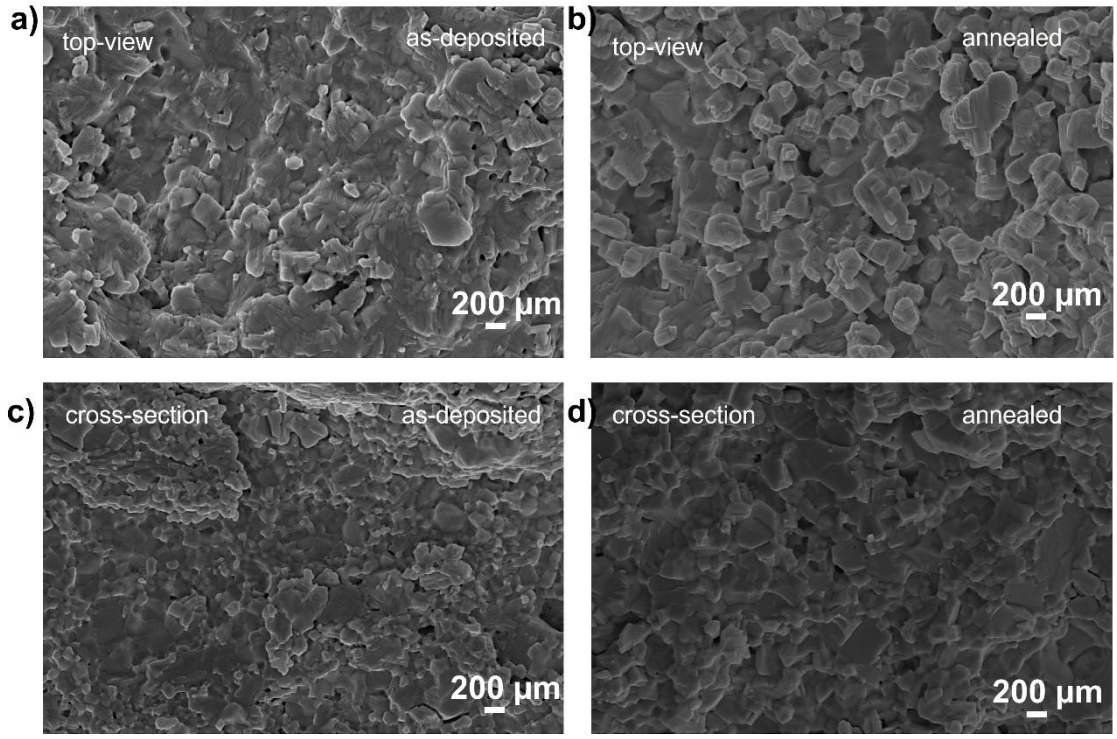

Fig. S15: SEM images of as-deposited and annealed PAD-MAPbBr$_3$ films on Al_2O_3 substrates (**a**,**b**: top-view; **c**,**d**: cross-section).

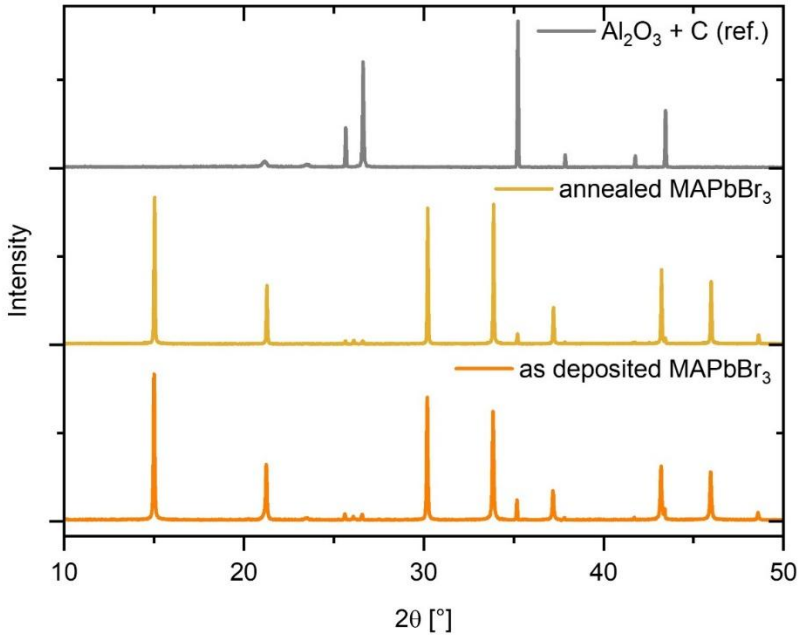

Fig. S16: XRD patterns of as-deposited and annealed PAD-MAPbBr$_3$ films on Al_2O_3 substrates with carbon IDE structure. The XRD pattern of the bare Al_2O_3/carbon IDE substrate is included for reference.

S5. Electrical Properties

Low-Frequency Impedance Response of $MAPbBr_3$: Evidence for Ionic-Dominated Conductivity

To further evaluate the electronic contribution to the measured conductivity, impedance spectra were measured over a frequency range extending down to 10^{-2} Hz. Carbon electrodes were employed in this work, acting as ion-blocking contacts at the $MAPbBr_3$/carbon interface. Probing this low-frequency regime enables access to the long-time response of the system, where ionic polarization is largely established and the remaining response is increasingly governed by electronic transport.

At intermediate frequencies, the impedance response reflects the mixed ionic–electronic nature of the material. In contrast, the Nyquist plot exhibits a characteristic transition from a Warburg-type diffusion feature to a pronounced low-frequency semicircle, as shown in **Fig. S17a**. Such behavior is commonly associated with stoichiometric and space-charge polarization under ion-blocking conditions, as reported for mixed ionic–electronic conducting systems [11–13]. In these systems, the low-frequency intercept on the real axis is commonly assigned to the electronic resistance (R_{eon}). The impedance spectra were fitted using the equivalent circuit shown in **Fig. S17b**.

From the fitting results, the low-frequency intercept corresponds to an electronic resistance of approximately 1.1×10^8 Ω, which is more than one order of magnitude larger than the resistance associated with the intermediate-frequency response (~5.3×10^6 Ω). This indicates that ionic transport dominates the overall conductivity, while the electronic contribution remains comparatively minor. Such behavior is consistent with the condition where the bulk chemical capacitance (C_δ) significantly exceeds the interfacial capacitance ($C_\perp$), leading to the observed Warburg-to-semicircle transition in the impedance spectrum.

Therefore, the measured conductivity (5.09×10^{-9} S cm^{-1} at 293 K) is considered to be predominantly governed by ionic transport.

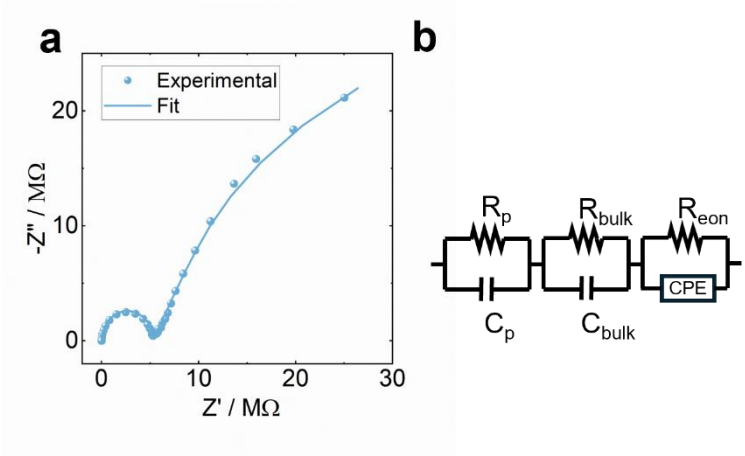

Fig. S17 a Nyquist plot of the annealed $MAPbBr_3$ film together with the fitted curve, measured down to 10^{-2} Hz at 323 K **b** Equivalent circuit model used for fitting the impedance spectra.

Effect of Annealing on the Impedance Response of $MAPbBr_3$ Films

It is well established that annealing at increasing temperatures can induce grain growth and modify defect densities in halide perovskite films. At the same time, ionic conductivity in these materials is often governed by halide point defects, such as vacancies or interstitials, which provide migration pathways for ions.

Fig. S18 presents the Nyquist plots measured at room temperature for a $MAPbBr_3$ film before and after annealing at 110 °C for 2 h. After annealing, the impedance spectra show an enlarged semicircle extending toward higher Z′ values together with a more pronounced low-frequency tail, indicating an increase in bulk resistance and a corresponding decrease in dark conductivity.

We note that the acquisition of a full temperature-dependent impedance dataset requires approximately 2 h. Since SEM images (**Fig. S15**) show noticeable grain growth after annealing, the pre-annealing step was used to minimize further thermally induced microstructural changes during the subsequent temperature-dependent impedance measurements. Consequently, the extracted activation energy, diffusion coefficient, and mobile ion concentration should be regarded as representative of a thermally stabilized (annealed state) microstructure rather than a pristine as-deposited state.

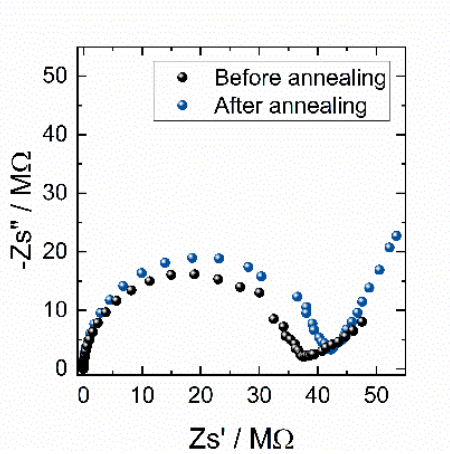

Fig. S18 Nyquist plots measured at room temperature for a $MAPbBr_3$ film before and after annealing at 110 °C for 2 h

Equivalent Circuit Modeling of Ionic Transport in $MAPbBr_3$

To quantitatively describe the impedance response, the experimental data were fitted using an equivalent circuit model composed of two Voigt elements and a constant phase element (CPE), as shown in **Fig. 9c**. Since both ionic and electronic transport in halide perovskites are typically thermally activated, the nearly temperature-independent response observed in the high-frequency region suggests that this feature is unlikely to originate from intrinsic charge transport processes in the $MAPbBr_3$ film. In addition, as shown in **Fig. S19,** the extracted capacitance values in the high-frequency range (5.5×10^4–10^6 Hz) fall within the range of 5–25 pF, which is characteristic of stray capacitive contributions. Therefore, this high-frequency response is mainly attributed to parasitic resistive and capacitive effects associated with the substrate, wiring, and measurement setup, and is represented by the first Voigt element. The second Voigt element describes the dominant thermally activated transport response of the $MAPbBr_3$ film. Owing to the small grain size and the resulting overlap of the characteristic time constants associated with grain-interior and grain-boundary transport, a single R–C element provides an effective description of their combined response. Finally, the low-frequency CPE is assigned to electrode polarization and ionic accumulation at the blocking interfaces.

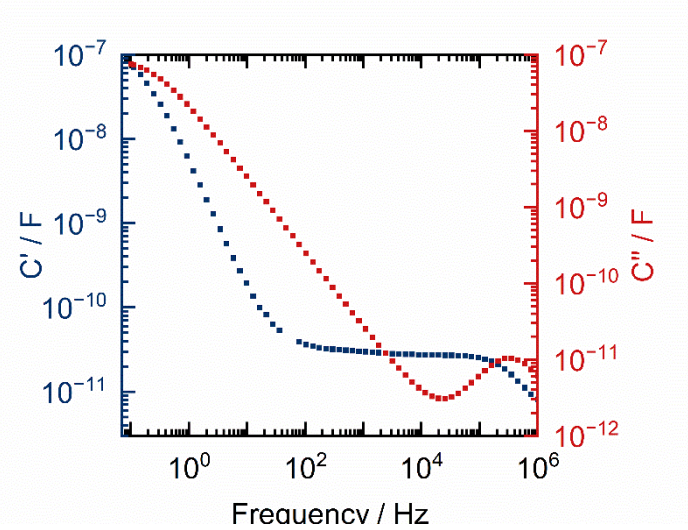

Fig. S19 Frequency dependence of the real (C′) and imaginary (C″) capacitance of $MAPbBr_3$ measured at 323 K up to 10^6 Hz

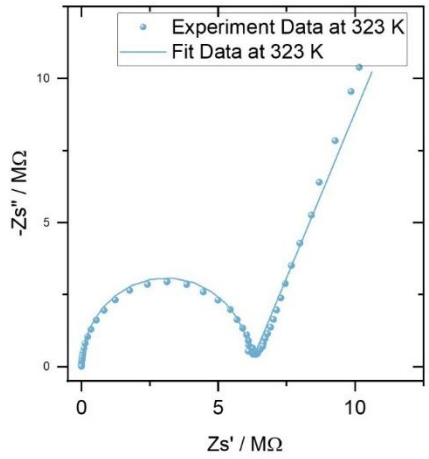

Fig. S20: Nyquist plot with fitted curves of annealed $MAPbBr_3$ film at 323 K.

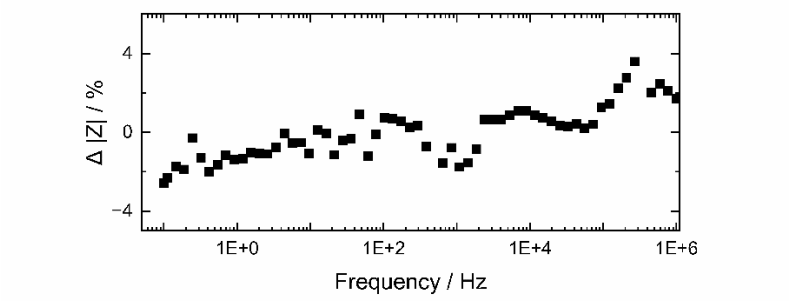

Fig. S21 Residual plot of the impedance magnitude (Δ|Z|) as a function of frequency obtained from Z-HIT analysis at 323 K.

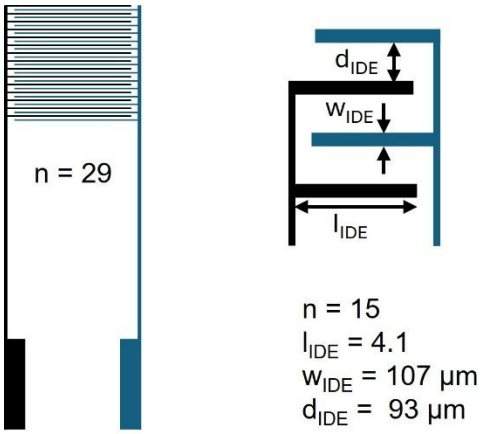

Fig. S22: Geometry and dimensional parameters of the interdigitated electrodes (IDE) used for electrical measurements.

The bulk conductivity σ_{bulk} was calculated according to the standard conductivity expression for an interdigitated electrode geometry:

$$\sigma_{bulk} = \frac{d}{R_{bulk} \cdot A} = \frac{1}{R_{bulk} \cdot [(2n-1) \cdot l \cdot t + 2n \cdot w \cdot t]} \quad \textbf{(Eq. S10)}$$

For film thicknesses exceeding 20 µm, the error associated with this approximation increases, as the electric field lines no longer pass homogeneously through the layer. For example, at a film thickness of 42 µm, the electrical conductivity is underestimated by approximately 20%. Therefore, the electrical conductivity was calculated using a thickness-dependent, simulation-based geometric factor F_{geo}, which is shown in **Fig. S23**.

$$\sigma_{bulk} = \frac{1}{R_{bulk} \cdot F_{geo}} \quad \textbf{(Eq. S11)}$$

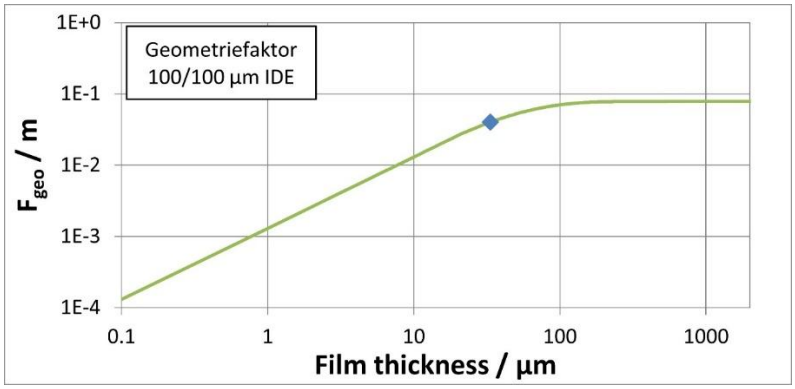

Fig. S23: Thickness-dependent geometric correction factor.

Dielectric Properties

The complex admittance $Y^*(\omega)$was calculated from the measured complex impedance $Z^*(\omega)$ according to:

$$Y^*(\omega) = \frac{1}{Z^*(\omega)} = \frac{1}{Z' + iZ''} = G(\omega) + iB(\omega) \quad \textbf{(Eq. S12)}$$

where $Z'$and $Z''$are the real and imaginary parts of the impedance. $G(\omega)$ and $B(\omega)$ denote the conductance and susceptance, respectively. These quantities are given by:

$$G(\omega) = \frac{Z'}{Z'^2 + iZ''^2} \quad \textbf{(Eq. S13)}$$

$$B(\omega) = \frac{-Z''^2}{Z'^2 + iZ''^2} \quad \textbf{(Eq. S14)}$$

The complex capacitance $C^*(\omega)$ was obtained from the admittance via

$$C^*(\omega) = \frac{Y^*(\omega)}{i\omega} \quad \textbf{(Eq. S15)}$$

yielding the real and imaginary components

$$C'(\omega) = \frac{B(\omega)}{\omega} \quad \textbf{(Eq. S16)}$$

$$C''(\omega) = \frac{G(\omega)}{\omega} \quad \textbf{(Eq. S17)}$$

To eliminate parasitic contributions, the corrected capacitance was calculated as:

$$C'_{corr}(\omega) = C'_{meas}(\omega) - C'_{leer}(\omega) \quad \textbf{(Eq. S18)}$$

where C'_{leer}represents the empty-cell capacitance. The sample capacitance is related to the dielectric permittivity by:

$$C_{sample} = \varepsilon_0(\varepsilon - 1)F_{geo} \quad \textbf{(Eq. S19)}$$

with ε_0 being the vacuum permittivity and $F_{\text{geo}}$the geometrical factor. Accordingly, the real and imaginary parts of the dielectric permittivity were calculated as:

$$\varepsilon'(\omega) = 1 + \frac{C'_{corr}(\omega)}{\varepsilon_0 F_{geo}} \quad \textbf{(Eq. S20)}$$

$$\varepsilon''(\omega) = \frac{C''_{corr}(\omega)}{\varepsilon_0 F_{geo}} \quad \textbf{(Eq. S21)}$$

To minimize the influence of low-frequency electrode polarization and charge transport related conductivity on the extracted parameters, the fitting was restricted to the frequency region around the tan delta peak.

$$\varepsilon^*(\omega) = \varepsilon'(\omega) - i\varepsilon''(\omega) \quad \textbf{(Eq. S22)}$$

$$\varepsilon^*(w) = \varepsilon_\infty + \frac{\Delta\varepsilon}{1 + (i\omega\tau)^{1-\alpha}} \quad \textbf{(Eq. S23)}$$

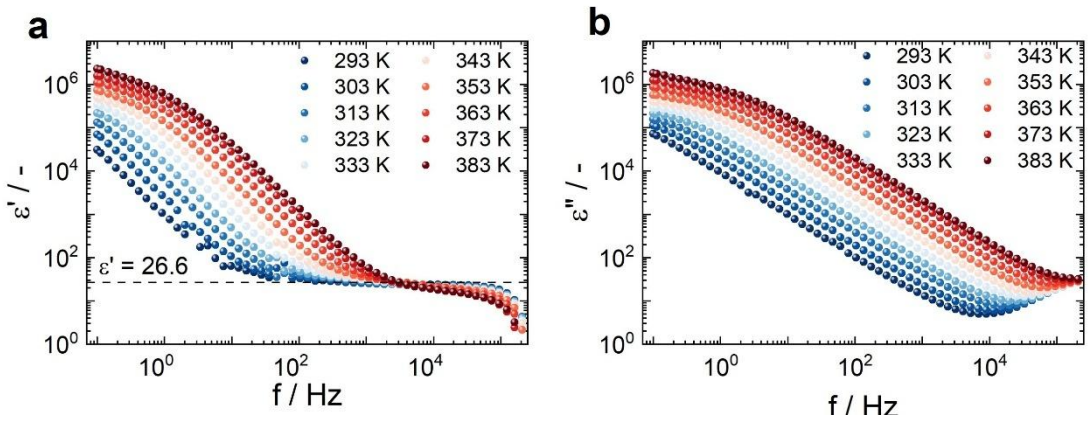

Figure S24: Temperature-dependent dielectric characteristics of annealed PAD-$MAPbBr_3$ film measured in the dark at temperatures ranging from 293 K to 383 K. **a** The real part of permittivity ε' with intrinsic bulk dielectric constant ($\varepsilon_{bulk} \approx 26.6$). **b** The imaginary part ε''.

S6. Diffusion Coefficient from tanδ Spectra

Under the assumption of a symmetric binary ionic conductor confined between ideally blocking electrodes, the Trukhan model predicts a characteristic relaxation associated with ionic diffusion, which manifests as a maximum in the loss tangent spectrum [14].

The maximum of loss tangent can be expressed as (Eq.21 in [14]):

$$\tan \delta_{\max} \approx \sqrt{\frac{\kappa \cdot L}{8}} \quad \textbf{(Eq. S24)}$$

Where κ is the inverse Debye length and L is the finger distance d_{IDE}. This relation holds for the case when $\kappa \cdot L$ >>1, which is valid in our case. The corresponding dimensionless frequency is given by (Eq.20 in [14]):

$$\Omega_{\max,\delta} \approx \sqrt{\frac{2}{\kappa \cdot L}} \quad \textbf{(Eq. S25)}$$

In our $MAPbBr_3$ film, the activation energy extracted from the conductivity is found to be comparable to that obtained from the characteristic relaxation frequency of the loss tangent. This consistency indicates that both charge transport and dielectric relaxation are governed by the same thermally activated ionic process. Furthermore, only a single relaxation peak is observed in the loss-tangent spectra over the entire investigated frequency and temperature range, suggesting the presence of a single dominant ionic relaxation mechanism.

Under these conditions, the $MAPbBr_3$ film can be effectively described by a single dominant ionic diffusion process. Consequently, the system can be mapped onto a symmetric binary ionic conductor within the Trukhan framework, leading to a simplified expression for the dimensionless frequency (Eq. B14 in [14]):

$$\Omega_{\max,\delta} \approx \frac{\omega_{max}^{tan\,\delta}}{\kappa^2 \cdot D} \quad \textbf{(Eq. S26)}$$

Accordingly, the diffusion coefficient can be written as:

$$D = \frac{\omega_{max}^{tan\,\delta}}{\kappa^2} \sqrt{\frac{\kappa \cdot L}{2}} \quad \textbf{(Eq. S27)}$$

By substituting **Eq. S24** into **Eq. S27** one obtains:

$$D = \frac{2\omega_{max}^{tan\,\delta} \cdot \tan \delta_{\max}}{\kappa^2} \quad \textbf{(Eq. S28)}$$

Finally, using **Eq. S24** again to replace κ, the diffusion coefficient can be expressed as:

$$D = \frac{\omega_{\max}^{\tan\delta} \cdot L^2}{32(\tan^3\delta)_{\max,\omega}} \qquad \textbf{(Eq. S29)}$$

References

[1] Katahara JK, Hillhouse HW (2014) Quasi-Fermi level splitting and sub-bandgap absorptivity from semiconductor photoluminescence. J Appl Phys 116. https://doi.org/10.1063/1.4898346

[2] Witt C, Schötz K, Köhler A, Panzer F (2024) Understanding method-dependent differences in Urbach energies in halide perovskites. J Phys Chem C 128:6336–6345. https://doi.org/10.1021/acs.jpcc.3c07293

[3] Wang W, Li Y, Wang X, Lv Y, Wang S, Wang K, Shi Y, Xiao L, Chen Z, Gong Q (2016) Density-dependent dynamical coexistence of excitons and free carriers in the organolead perovskite CH3NH3PbI3. Phys Rev B 94. https://doi.org/10.1103/PhysRevB.94.140302

[4] Burstein E (1954) Anomalous optical absorption limit in InSb. Phys Rev 93:632–633. https://doi.org/10.1103/PhysRev.93.632

[5] Moss TS (1954) The interpretation of the properties of indium antimonide. Proc Phys Soc B 67:775–782. https://doi.org/10.1088/0370-1301/67/10/306

[6] D'Innocenzo V, Srimath Kandada AR, de Bastiani M, Gandini M, Petrozza A (2014) Tuning the light emission properties by band gap engineering in hybrid lead halide perovskite. J Am Chem Soc 136:17730–17733. https://doi.org/10.1021/ja511198f

[7] Droseros N, Longo G, Brauer JC, Sessolo M, Bolink HJ, Banerji N (2018) Origin of the enhanced photoluminescence quantum yield in MAPbBr3 perovskite with reduced crystal size. ACS Energy Lett 3:1458–1466. https://doi.org/10.1021/acsenergylett.8b00475

[8] Yang Y, Yang M, Li Z, Crisp R, Zhu K, Beard MC (2015) Comparison of recombination dynamics in CH3NH3PbBr3 and CH3NH3PbI3 perovskite films: Influence of exciton binding energy. J Phys Chem Lett 6:4688–4692. https://doi.org/10.1021/acs.jpclett.5b02290

[9] Duijnstee EA, Le Corre VM, Johnston MB, Koster LJA, Lim J, Snaith HJ (2021) Understanding dark current-voltage characteristics in metal-halide perovskite single crystals. Phys Rev Applied 15. https://doi.org/10.1103/PhysRevApplied.15.014006

[10] Yuan Y, Yan G, Dreessen C, Rudolph T, Hülsbeck M, Klingebiel B, Ye J, Rau U, Kirchartz T (2024) Shallow defects and variable photoluminescence decay times up to 280 µs in triple-cation perovskites. Nat Mater 23:391–397. https://doi.org/10.1038/s41563-023-01771-2

[11] Bumberger AE, Nenning A, Fleig J (2024) Transmission line revisited – the impedance of mixed ionic and electronic conductors. Phys Chem Chem Phys 26:15068–15089. https://doi.org/10.1039/D4CP00975D

[12] Moia D, Jung M, Wang YR, Maier J (2023) Ionic and electronic polarization effects in horizontal hybrid perovskite device structures close to equilibrium. Phys Chem Chem Phys 25:13335–13350. https://doi.org/10.1039/D3CP01182H

[13] Maier J (2023) Physical chemistry of ionic materials: Ions and electrons in solids. Wiley, Hoboken, NJ. ISBN 978-1-119-79910-8

[14] Sørensen TS, Compañ V (1995) Complex permittivity of a conducting, dielectric layer containing arbitrary binary Nernst–Planck electrolytes with applications to polymer films and cellulose acetate membranes. J Chem Soc Faraday Trans 91:4235–4250. https://doi.org/10.1039/FT9959104235